Journal of Materials Chemistry C

ROYAL SOCIETY OF CHEMISTRY

PAPER

View Article Online
View Journal

Cite this: DOI: 10.1039/d5tc01418b

Electroactive naphthalimide and naphthalenediimide interlayers for inverted perovskite solar cells

Konstantina-Kalliopi Armadorou, †[a] Ghewa AlSabeh, †[ab] Andrea Vezzosi, †[c] Murad Najafov,[b] Pietro Nasturzio,[a] Paul Zimmermann,[d] Alexander Hinderhofer,[d] Jinhyun Kim,[a] Likai Zheng,[a] Tiziano Agostino Caldara,[a] Virginia Carnevali,[c] Vladislav Slama,[c] Nikolaos Lempesis,[ce] Frank Schreiber,[d] Shaik M. Zakeeruddin,[a] Ursula Rothlisberger,[c] Lukas Pfeifer,[a] Felix T. Eickemeyer,*[a] Jovana V. Milić *[abf] and Michael Grätzel*[a]

Received 5th April 2025,
Accepted 1st August 2025

DOI: 10.1039/d5tc01418b

rsc.li/materials-c

Perovskite solar cells have garnered significant interest, yet their limited operational stability remains a major challenge. This is especially pronounced at the interface with charge transport layers. In inverted p–i–n perovskite solar cells, fullerene-based electron transport layers pose critical stability issues. This has stimulated the application of low-dimensional perovskite interlayers featuring alkylammonium-based organic spacers that template perovskite slabs to enhance operational stabilities. However, these materials are traditionally based on organic cations that are electronically insulating, limiting charge extraction and device performance. We demonstrate the capacity to access low-dimensional perovskites incorporating electron-accepting naphthalimide- and naphthalenediimide-based spacers and use the corresponding organic moieties to modify or replace fullerene electron-transport layers, forming an electroactive interface that serves charge-transport. This resulted in superior performance with power conversion efficiencies exceeding 20% and enhanced operational stability, highlighting the potential of electroactive interlayers for advancing inverted perovskite solar cells.

Introduction

Lead halide perovskites have attracted increasing attention in the past decade for their application in optoelectronic devices.[1] This progress stems from their unique optoelectronic and optoionic properties, including a tuneable bandgap, high absorption coefficients, a small exciton binding energy, as well as high carrier mobilities, long carrier diffusion lengths and lifetimes.[2–6] The combination of these characteristics with their ease of processing from solution has resulted in an enhancement in power conversion efficiency (PCE) from 3.8% to above 26% in perovskite solar cells (PSCs).[7,8] However, the inherent instability of lead halide perovskites during operation due to interfacial reactivity and ion migration,[9,10] along with their sensitivity to environmental factors, can induce further degradation,[11] especially at the interface between the perovskite and charge transport layers in solar cells, hampering their practical application.[12] The emergence of low-dimensional (LD) perovskites has provided an alternative to addressing this challenge.[13,14] They are based on bulky organic cations templating inorganic perovskite slabs,[13,14] which exhibit enhanced stability compared to their three-dimensional analogues[15–17] owing to the hydrophobic nature of the organic moieties, their interactions, and reduced ion migration.[18–20] However, the insulating nature of most organic moieties to date hinders electronic conductivity, thus reducing PSC efficiency.[21] Furthermore, a significant factor in achieving high power conversion efficiency and stability in PSCs is the suitability of charge transport layers, namely the electron transport layer (ETL) and the hole transport layer (HTL). This is especially important in the case of inverted (p–i–n) PSCs, wherein the most commonly used ETLs are organic fullerene-based materials,

[a] Laboratory of Photonics and Interfaces, Institute of Chemical Sciences and Engineering, École Polytechnique Fédérale de Lausanne, 1015 Lausanne, Switzerland. E-mail: felix.eickemeyer@epfl.ch, michael.graetzel@epfl.ch
[b] Smart Energy Materials, Adolphe Merkle Institute, University of Fribourg, 1700 Fribourg, Switzerland. E-mail: jovana.milic@unifr.ch
[c] Laboratory of Computational Chemistry and Biochemistry, Institute of Chemical Sciences and Engineering, École Polytechnique Fédérale de Lausanne, 1015 Lausanne, Switzerland
[d] Institut für Angewandte Physik, Universität Tübingen, 72076 Tübingen, Germany
[e] Department of Chemistry, University of Ioannina, 45110 Ioannina, Greece
[f] Department of Chemistry, University of Turku, 20900 Turku, Finland
† These authors contributed equally to this work.

primarily [6,6]-phenyl-C_{61}-butyric acid methyl ester (PCBM) or C_{60}.[22] PCBM suffers from severe stability limitations due to its low relative permittivity, photo-oxidation, and formation of electron-trapping moieties under illumination.[23,24] Moreover, using C_{60} is more costly due to the challenging separation of fullerene homologues.[25] Another limitation is the highly defective perovskite/fullerene interface in p–i–n PSCs featuring trap-mediated non-radiative recombination, affecting both the efficiency and stability of solar cells.[26] To address these critical limitations, improving the interface between the perovskite and the fullerene-based electron transport layer is critical, and the employment of functional molecules that serve both as passivating agents and electron transport layers is relevant.[27–29] Another strategy involves the development of organic moieties that can act as LD or 2D perovskite layers with a simultaneously passivating and stabilising effect. Their integration with functional electroactive components between the perovskite and charge-transport interface has the potential to overcome performance limitations by facilitating charge transport,[14] which remains underexploited in inverted perovskite solar cells. To this end, organic electron acceptors such as perylene- and naphthalenediimide-based polymers and small molecules have been explored due to the ease of processing from solution and structural versatility.[30,31] However, their potential to form LD perovskite phases that enhance device stability and performance in photovoltaics remains unexploited.

Here, we introduce electroactive naphthalimide (NI) and naphthalenediimide (NDI) derivatives at the interface between the hybrid lead halide perovskite absorber and the fullerene-based ETL in inverted PSCs. These electron-accepting organic materials[32,33] have been shown to feature unique optoelectronic properties, such as charge-transfer-induced photoluminescence quenching[34,35] and phosphorescence.[36,37] Their modular structure and the capacity to form low-dimensional perovskite phases stimulated prior investigations,[35,38] yet without the use in photovoltaics. We further explore their functionality in inverted perovskite solar cells at the interface with the electron-transport layers and elucidate their function using density functional theory (DFT) and *ab initio* molecular dynamics (AIMD). While NI was shown to act as an interfacial defect passivator, NDI operated as a charge transfer facilitator to the ETL. This resulted in higher performances of fullerene-based solar cell devices with enhanced operational stability. Furthermore, we show the feasibility of engineering fullerene-free devices with insights into material and device design.

Results and discussion

Electroactive low-dimensional perovskite materials

We studied two organic moieties based on extended aromatic cores featuring electron-accepting properties,[31,39] including 2-(1,3-dioxo-1*H*-benzo[*de*]isoquinolin-2(3*H*)-yl)ethan-1-ammonium iodide (NI; Fig. 1(a)) and 2,2′-(1,3,6,8-tetraoxo-1,3,6,8-tetrahydrobenzo[*lmn*][3,8]phenanthroline-2,7-diyl)bis(ethan-1-ammonium) iodide (NDI; Fig. 1(b)). They were designed based on the electron-withdrawing naphthalene core functionalised with the ethylammonium groups to induce 2D perovskite formation. The organic cations were synthesised *via* a two-step reaction adapting previously reported procedures, as described in the SI (Fig. S1–S8).[32,33] Specifically, carboxylic anhydrides are transformed into the *Boc*-protected ethylammonium imides, yielding the resulting monofunctional (NI) and bifunctional (NDI) ammonium iodide salts upon deprotection and protonation. Thin films of the target molecules and the respective LD perovskites were prepared based on S_xPbI_4 (n = 1) and $S_xFAPb_2I_7$ (n = 2) nominal compositions (S = NI, NDI with x = 1 for NDI and x = 2 for NI) by mixing the stoichiometric amounts of precursor materials by solution-processing, followed by annealing (as described in the Experimental Section of the SI). The monofunctional NI is expected to form 2D Ruddlesden–Popper (RP) phases, while the bifunctional NDI 2D Dion–Jacobson (DJ) halide perovskites.[32,33] We analysed their n = 1–2 nominal compositions to assess the capacity to form LD or layered (2D) perovskite phases.

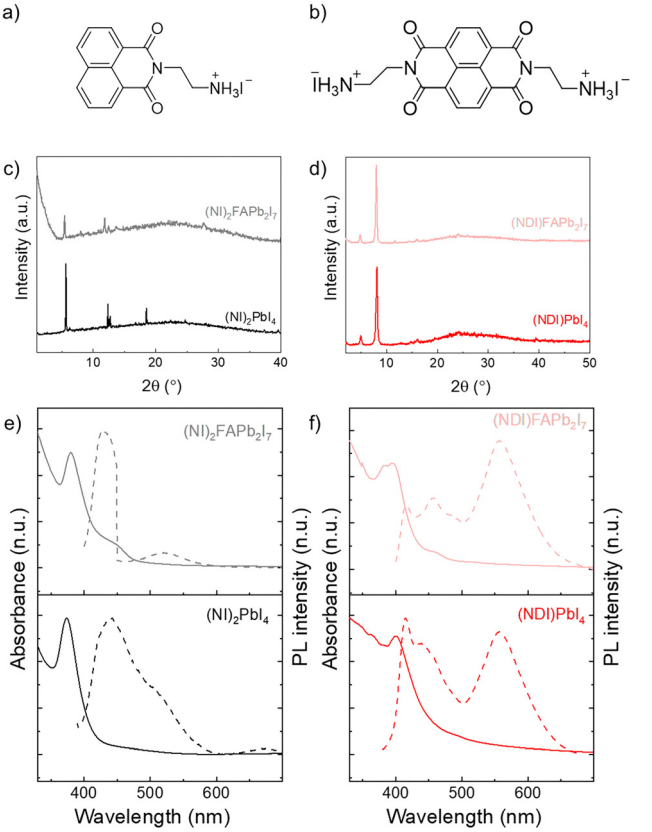

Fig. 1 Structural and optoelectronic properties of naphthal(enedi)imide LD perovskites. (a) and (b) Structural representations of NI and NDI. (c) and (d) XRD patterns of films of (c) $(NI)_2PbI_4$, $(NI)_2FAPb_2I_7$, (d) $(NDI)PbI_4$, and $(NDI)FAPb_2I_7$ nominal compositions. (e) and (f) UV-Vis (full line) and PL (dashed line) spectra of films based on (e) $(NI)_2PbI_4$, $(NI)_2FAPb_2I_7$, (f) $(NDI)PbI_4$, and $(NDI)FAPb_2I_7$ nominal compositions on glass.

X-ray diffraction (XRD) of the corresponding thin films revealed peaks at low angles (below 10°) corresponding to the LD perovskite phases.[40,41] Moreover, a periodic pattern, typical of 2D perovskite structures, was observed for n = 1 $(NI)_2PbI_4$ and $(NDI)PbI_4$ compositions (Fig. 1(c) and (d)). For the n = 2 compositions, lower crystallinity was observed along with the

presence of peaks related to the co-existing $n = 1$ phase ($\sim 5.7^\circ$ in (NDI)$FAPb_2I_7$), excess PbI_2 ($\sim 12.6^\circ$) and 3D perovskite ($\sim 14.8^\circ$) phases (Fig. 1(c) and (d)), which were further analysed by using grazing-incidence X-ray scattering (GIWAXS) measurements (Fig. S9 and S10). For the $(NI)_2PbI_4$ ($n = 1$) composition, the first peak associated with the LD phase was oriented parallel to the substrate. However, a polymorph was also present, oriented in a different direction. The $(NI)_2FAPb_2I_7$ ($n = 2$) composition, on the other hand, was randomly oriented. Both NDI compositions were oriented parallel to the substrate. Additionally, neither the NI nor the NDI $n = 2$ nominal compositions showed any additional peaks to those of the $n = 1$ phase, suggesting $n = 2$ phase did not form.

The capacity to form LD perovskite phases was further assessed by DFT calculations. DFT optimizations of $n = 1$ (NDI)PbI_4 model systems corroborate the formation of a 2D DJ perovskite structure for the $n = 1$ (NDI)PbI_4 composition (Fig. S11a). The comparison of simulated and experimental XRD patterns indicates that the peak around 8° is likely related to the presence of LD δ-$FAPbI_3$-like structure where the FA cations are replaced by NDI molecules (Fig. S12 and S13). Moreover, for the $n = 1$ $(NI)_2PbI_4$ composition, simulated XRD spectra relate the peak at $\sim 5.7^\circ$ (Fig. 1(c)) to the formation of a 1D phase with the typical structure of δ-$FAPbI_3$ phase involving NI molecules replacing the FA cations (Fig. S14). The calculated 2D RP $n = 1$ $(NI)_2PbI_4$ phase (Fig. S11b) features a Pb–Pb interlayer distance of 23 Å corresponding to a low peak at 3.8° that does not match the experimental XRD spectra (Fig. S12b). This suggests that the NI-based system forms a 1D perovskite phase instead.

The optical properties of the thin films were further analysed using UV-vis and PL spectroscopy (Fig. 1(e) and (f)). UV-vis spectra show excitonic peaks in the 350–450 nm range, characteristic of LD perovskite.[42,43] For $(NI)_2PbI_4$ composition, a peak at 373 nm was observed, which was red-shifted to around 380–400 nm for $(NI)_2FAPb_2I_7$ nominal composition. A comparable absorbance band around 400 nm was observed for (NDI)PbI_4 and (NDI)$FAPb_2I_7$ compositions, with the latter exhibiting an additional signal at 450 nm. However, the formation of $n = 2$ for either NI or NDI composition was not evident from the XRD or GIWAXS under the applied experimental conditions. Similarly, additional spectral features could not be associated with pure organic spacers or their (*i.e.*, dimer) assemblies. PL spectra showed a maximum emission peak at 440 nm for $(NI)_2PbI_4$ that was shifted to 430 nm for the $(NI)_2FAPb_2I_7$, with the emergence of a peak at around 520 nm. For the NDI systems, several peaks were observed in the range of 400–650 nm, with a maximum at 550 nm, suggesting a mixture of LD phases in accordance with previous reports.[44]

In summary, structural and optoelectronic characteristics combined with theoretical investigation suggest that NI and NDI moieties form LD perovskite phases, which may involve 2D phases for the NDI system yet predominantly include 1D phases for the NI system. Their functionality was thereafter further assessed at the interlayer with the 3D perovskites.[45]

Effect of electroactive layers on 3D perovskites

To understand the effect of electroactive organic spacers in perovskite heterostructures, films based on conventional triple-cation halide perovskites, $(Cs_{0.05}MA_{0.05}FA_{0.9}Pb(I_{0.95}Br_{0.05})_3)$ compositions were deposited on glass substrates according to the reported procedures described in the SI. NI and NDI were thereafter deposited from a mixture of methanol, isopropanol and toluene (0.2 mg mL^{-1}), and the resulting films were compared to the neat (untreated) 3D perovskite samples.

XRD patterns show no change upon deposition of the NDI/NI overlayer (Fig. S15), indicating the preservation of the 3D perovskite structure. There were no apparent peaks below 10°, which would indicate LD overlayer formation, which can likely be attributed to the low concentration used. This was further analysed by X-ray photoelectron spectroscopy (XPS; Fig. S16), showing that Pb $4f_{7/2}$ and $4f_{5/2}$ peaks at 138.77 and 143.66 eV, respectively, remained unchanged upon treatment (Fig. S16a). The same applies to the N 1s spectra (Fig. S16b), which reveal a peak at 400.90 eV across all samples, corresponding to FA and possibly NDI in the films, whereby NI-treated samples show an additional peak at 402.60 eV that could be attributed to the ammonium groups in a new environment. GIWAXS measurements were thus used to assess the perovskite heterostructures (Fig. S17 and S18), which showed no significant change in the composition or crystallographic orientation upon applying the overlayer. In particular, they featured a mostly random orientation with a preference towards 35° and 65° tilt towards the surface. Radial profiles show that the films consist almost exclusively of α-phase perovskite, in addition to a very small amount of δ-phase evidenced at approximately 0.85 $Å^{-1}$. The local structure of the materials was further examined using solid-state NMR spectroscopy of polycrystalline powders (Fig. S19).[46,47] To achieve high detection sensitivity, we used powders of the 3D perovskite, both with and without NI and NDI, synthesised by mechanosynthesis.[48] A comparison of the ^{13}C NMR spectra of the 3D perovskites containing spacers with those of the neat NI and NDI precursors revealed slight changes in the $-CH_2-$ region (45–50 ppm), the aromatic (Ar) (120–150 ppm), and the FA region (155–160 ppm), corresponding to the formation of new haloplumbate phases. These changes imply a difference in the local structure or geometry of the spacers and FA cations in the hybrid perovskite.

The local structure of the interlayer can play an important role in the optoelectronic properties, and the theoretical investigations of NDI and NI moieties as overlayers onto 3D perovskite were used to understand their interactions. The binding energies of NDI^{2+} and NI^+, relative to the binding energy of two and one FA^+, respectively, were computed at the quantum mechanical level and found to be -0.45 eV for NDI^{2+} in the parallel configuration, -0.18 eV for NDI^{2+} in the diagonal configuration, and -0.17 eV for NI^+ (as detailed in the Experimental section of the SI). Both NDI and NI show stronger binding energies than FA, indicating their stable binding to the perovskite surface and a tendency to replace FA, thereby promoting surface coverage. Each NDI molecule binds to the $FAPbI_3$ surface by replacing two FA cations with its two

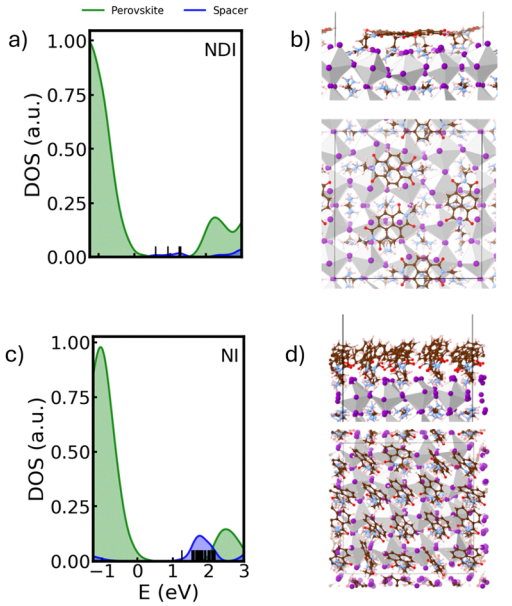

Fig. 2 Theoretical structure and optoelectronics of electroactive NDI/NI layers. Calculated projected density of states (PDOS) for perovskite (green) and molecular (blue) states for NDI (a) and NI (c) acting as overlayers on top of a 3D $FAPbI_3$ perovskite with corresponding top and side views of the molecular structures in (b) and (d), respectively. In (a) and (c) the energy is referenced to the calculated Fermi level (set to 0 eV), which corresponds to the calculated HOMO level of the system. For the specific structures in (b) and (d), a 40% higher surface coverage was calculated for the NI-passivated surface compared to its NDI-treated counterpart (Fig. S20 and S21).

ammonium groups (Fig. 2(b)). Consequently, the organic part of the molecule lays flat on the surface. On the contrary, each NI molecule binds to the perovskite by replacing one FA vacancy and, consequently, can orient almost vertically on top of the perovskite surface (Fig. 2(d)). This differentiates the surface properties of the two systems; while NI molecules can form a dense monolayer, in the NDI-treated surface, steric repulsion between different flat-laying molecules limit the maximum allowed number of units per surface area and their respective arrangement. This has an impact on the corresponding surface coverage and the electronic properties of the resulting material.

To assess the charge transport properties of the NDI and NI moieties, we calculated the projected density of states (PDOS; Fig. 2(a) and (c), corresponding to the structures in Fig. 2(b) and (d)). Overall, NDI is expected to have faster charge extraction than NI due to its proximity to the perovskite surface and flat orientation, which implies a vertical orientation of the aromatic p_z-molecular orbitals of the conjugated ring system. This is further supported by the calculated higher gas-phase electron affinity (EA) of NDI compared to NI (Table S1). However, the NDI overlayer introduces a series of states within the perovskite bandgap (Fig. 2(a)), corresponding to the LUMO states of the organic moiety. These states are primarily localised on the π-conjugated system of the NDI (Fig. S22b and S23). The localised mid-gap states are expected to enhance non-radiative recombination at the interface by trapping electrons and impeding further transport to the ETL. On the other hand, the NI molecular overlayer introduces a set of states distributed in a range of ~0.9 eV below the perovskite conduction band (Fig. 2(c)), which stem from LUMO levels of the spacers and are mainly localised on the molecular layer (Fig. S24b and S25). Due to the almost vertical orientation of the NI, the p_z orbitals of these states have an almost parallel orientation with respect to the perovskite surface. This further impacts interface energetics, which can be assessed by comparing the work function changes upon treatment with NI and NDI (Fig. S26). In both cases, the overlayer lowers the work function of the 3D perovskite due to interfacial dipoles, with the effect being more pronounced for NI than for NDI. Ultraviolet photoelectron spectroscopy (UPS) measurements (Fig. S27) corroborate this trend, revealing work-function reductions of 0.47 eV (NI) and 0.04 eV (NDI) relative to pristine films, in qualitative agreement with our PBE/PBE0 estimates (−2.21/−2.42 eV for NI and −0.54/−0.53 eV for NDI). The quantitative gap likely stems from the use of spacer-modified perovskites rather than neat spacer layers, the effects of the surface coverage, and model simplification. Such lowering of the work function,[49,50] is expected to affect photovoltaic characteristics.

Photovoltaic characteristics

The photovoltaic performance was assessed in the inverted p–i–n device configuration of fluorine-doped tin oxide (FTO)/[2-(3,6-dimethoxy-9*H*-carbazol-9-yl)ethyl]phosphonic acid (MeO-2PACz)/$Cs_{0.05}MA_{0.05}FA_{0.9}Pb(I_{0.95}Br_{0.05})_3$ (~400 nm)/[6,6]-phenyl-C_{61}-butyric acid methyl ester (PBCM) – bathocuproine (BCP) (~180 nm)/Ag (~120 nm) with and without overlayers at the interface between the perovskite and the ETL (Fig. 3 and Table S2). The neat and NDI/NI treated devices were compared to those prepared using electronically inactive 1,3-propane-diammonium (PDA) iodide, a standard interface defect passivator for high-

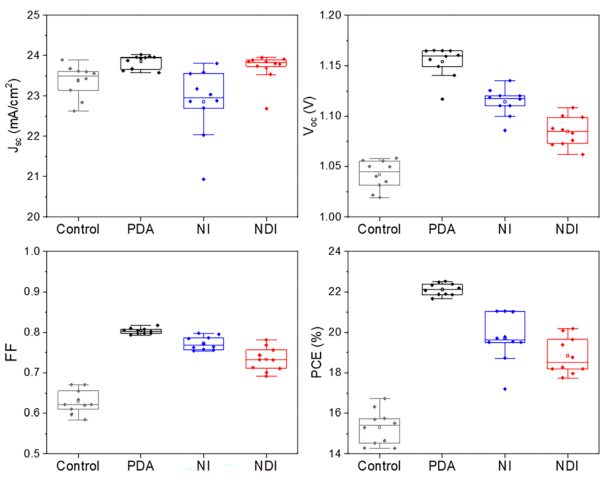

Fig. 3 Photovoltaic characteristics of inverted perovskite solar cell devices. Photovoltaic metrics of control (gray) and modified devices with PDA (black), NI (blue) and NDI (red) interlayers based on $Cs_{0.05}MA_{0.05}FA_{0.9}Pb(I_{0.95}Br_{0.05})_3$ perovskite compositions and (FTO)/MeO-2PACz/$Cs_{0.05}MA_{0.05}FA_{0.9}Pb(I_{0.95}Br_{0.05})_3$/PBCM-BCP/Ag device architecture.

performance inverted perovskite solar cells.[49,50] The concentration of PDA was kept constant (at 0.5 mg mL^{-1}) based on previous reports,[51] whereas the concentrations of NI and NDI were optimised to be 0.2 mg mL^{-1} and 0.1 mg mL^{-1}, respectively, based on performance and solubility. The two conditions showed performances above 20% PCE for champion devices (21.1% for NI, 20.2% for NDI), slightly below the PDA-modulated champion cell (22.5%), with the possibility to further optimise being beyond the scope of this study.[49] Overall, NI and NDI treatment enhanced open-circuit voltages (V_{oc}) with an average of 73 mV and 44 mV, respectively, with a simultaneous increase of the fill-factor (FF) by 14% and 10% average, respectively. A stable output for the modulated devices during maximum power point tracking (MPP) for one minute under one sun illumination was confirmed (Fig. S28). Furthermore, no shift in the onset of the incident photon-to-current conversion efficiency (IPCE) was detected for the target devices, while the integrated current densities agree with the J_{sc} values from the current–voltage (J–V) characteristics (Fig. 4(a) and (b)).

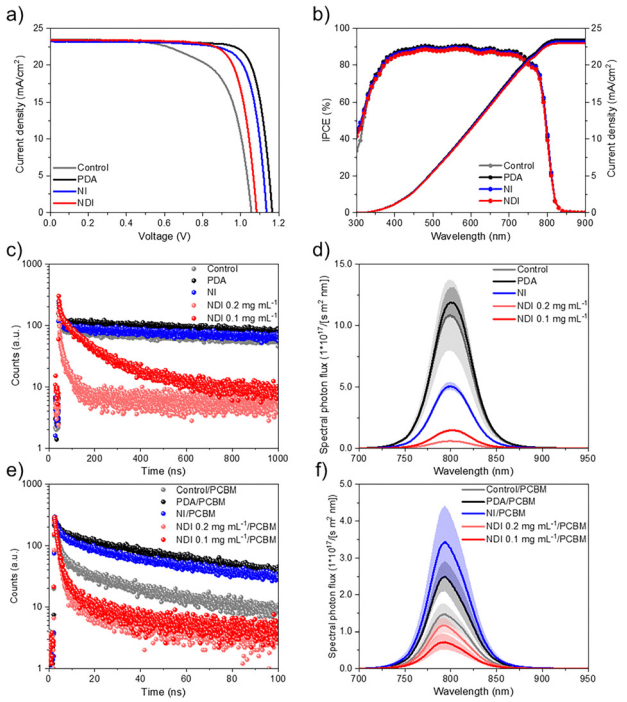

Fig. 4 Optoelectronic characteristics of NI/NDI-based perovskite solar cells. (a) J–V curves of the devices with different passivation layers in comparison to the control device without any treatment, with a scan rate of 10 mV s^{-1}. (b) IPCE spectra and calculated photocurrent integrated over the standard AM 1.5 G solar spectrum. In agreement to the J–V data no change in the spectra is observed. (c) and (e) Time-resolved photoluminescence spectroscopy (TRPL) of perovskite (gray) and modulated films with PDA (black), NI (blue), NDI high concentration (pink) and NDI low concentration (red) on microscope slides without (c) and with (e) the electron-transport material (PCBM). (d) and (f) Steady-state absolute intensity photoluminescence (AIPL) spectra of perovskite (gray) and treated films with PDA (black), NI (blue), NDI (high concentration, pink, and low concentration, red) on FTO/MeO-2PACz without (d) and with (f) the electron-transport layer (PCBM). Error band represents the standard deviation of 5 samples per condition.

Factors influencing the photovoltaic performance were investigated by steady-state absolute intensity photoluminescence (AIPL) spectroscopy and time-resolved photoluminescence (TRPL) spectroscopy.[52,53] TRPL measurements were performed on control and overlayer-modified films on glass, with and without the fullerene ETL. In the control, PDA-modified, and NI-modified films without fullerene ETL, the commonly observed rapid PL decay within the first 10 ns (Fig. 4(c)) corresponds to the initial rapid localisation of charge carriers due to trap filling. This is followed by non-radiative charge carrier recombination,[54] indicating µs-range carrier lifetimes.[55] In contrast, the NDI-modified films exhibit a significantly more pronounced initial fast PL decay within the first 100 ns, indicating electron injection from the conduction band of the perovskite film to the LUMO level of NDI, corroborating theoretical calculations and suggesting that NDI does not act as a barrier for charge extraction. This is in accordance with the UPS data (Fig. S27) as the conduction-band minimum (CBM) is 0.13 eV below the pristine perovskite CBM (−3.73 eV), providing a downhill pathway for electron extraction. In contrast, NI shifts the CBM upward to −3.54 eV, introducing a ∼0.2 eV barrier for charge extraction.

This is further supported by the less pronounced initial PL decay observed with decreasing overlayer thickness (Fig. 4(c)), attributed to a reduced availability of empty states for electron transfer. The AIPL data of the films on FTO/MeO-2PACz revealed an emission peak at ∼800 nm, with a photoluminescence quantum yield (PLQY) of 3.5% for the control, which is three times greater than the NI-modified samples (1.6%) and more than one order of magnitude greater than that of the NDI-modified samples (0.2%) (Fig. 4(d) and Table S3). The reduced PLQY indicates enhanced non-radiative recombination caused by mid-gap states at the perovskite/NI and perovskite/NDI interfaces, as evidenced by the DFT calculations (Fig. 2(a) and (c)). The significantly lower PLQY observed for NDI can be attributed to its much stronger interaction with the perovskite, which results in a higher surface recombination. In contrast, an increase in the PLQY can be noticed for the PDA-modified films (3.8%), indicating suppressed non-radiative recombination.[49] The introduction of PCBM leads to comparable observations in the TRPL data, where the NDI-modified samples exhibit a more pronounced initial decay compared to both the control and the modified films without PCBM due to the additional electron injection into the fullerene layer (Fig. 4(e)), which is likely enabled by the localised mid-gap states of NDI and the close proximity of PCBM in π-stacking contact with NDI (Fig. S29b). The NI-modified films show less pronounced electron injection into the PCBM, most likely due to their vertical orientation and larger distance between the surface and PCBM (Fig. 2(d), Fig. S29c, and Table S4). The addition of PCBM leads to a decrease in the PLQY by almost one order of magnitude in all films, except for NI-modified samples where the PLQY decrease is not as significant (Fig. 4(f) and Table S3), with a more pronounced decrease in the control film (0.5%) due to the increased number of surface defects.[12] Interfacial treatment with NI leads to an increase in the PLQY (1.1%) due to a Fermi-level upshift and reduced non-radiative recombination, even

when compared with the PDA-based films (0.8%). Finally, the decrease of PLQY in the presence of NDI (0.4%) further corroborates its electroactive role, acting as a mediator for deep surface trap states, differentiating it from other organic molecules with passivating properties.

To further understand the interaction with the ETL, we performed *ab initio* molecular dynamics simulations of a model system comprising one PCBM molecule interacting with control as well as NDI and NI-treated $FAPbI_3$ surfaces. NI forms a thicker monolayer at the $FAPbI_3$ surface (Fig. 2d top), which increases the distance between the PCBM and the perovskite surface compared to NDI (Fig. S29 and Table S4). The thin PCBM–$FAPbI_3$ interlayer separation in the presence of the NDI and the close contact of the C_{60} system with the π-orbitals of the NDI molecules (*ca.* 3.6 Å close to π–π stacking distance) can explain a better electron injection compared to NI. The calculations of the interaction enable rationalising the observed percentage of PLQY reduction for NI/$FAPbI_3$ and NDI/$FAPbI_3$ after the introduction of the PCBM layer (*ca.* 85% and 10% for NDI and NI, respectively). Specifically, PLQY reduction for the NDI-based treatment is comparable to that of the control (90%) and that of PDA/$FAPbI_3$ (80%), which can be attributed to a thinner PCBM–$FAPbI_3$ interlayer separation and NDI orientation.

This mode of interaction and the corresponding electronic characteristics of NDI could enable it to act as selective electron-extraction material. To assess this perspective, we fabricated fullerene-free devices with atomic-layer deposition of tin oxide (ALD-SnO_2) on top of the target interlayer-modulated perovskite layer. Interestingly, in contrast to NI and PDA, the NDI interlayer leads to an operational device (Fig. S30, S31 and Table S5), achieving over 12% PCE in the champion cell, with photovoltaic parameters of 22.78 mA cm^{-2} for J_{sc}, 0.99 V for V_{oc} and 0.51 for FF. These findings showcase that a fullerene-free p–i–n device was fabricated, offering the potential to address the stability and cost concerns.

Simulation of the interface considering $FAPbI_3$(FAI-terminated)/SnO_2, $FAPbI_3$(PbI-terminated)/SnO_2, $FAPbI_3$/NDI/SnO_2 and NI/SnO_2 model systems show a difference based on electron density redistribution (Fig. S32). The Bader charge analysis suggests that electrons flow from $FAPbI_3$ to SnO_2 (Fig. S33). In the case of $FAPbI_3$/SnO_2, charge redistribution mainly affects the polarisation of the halogen ions at the interface. On the other hand, when NDI or NI mediate the $FAPbI_3$–SnO_2 interaction, the systems show two oppositely charged layers at the interface. This generates an interface dipole, which results in a built-in electric field pointing from SnO_2 to $FAPbI_3$, which favours electron extraction (Fig. S34) and modifies the energy band alignment close to the Fermi level (Fig. 5). The $FAPbI_3$/SnO_2 and $FAPbI_3$/NDI/SnO_2 interfaces show a type-II energy level alignment, which should be advantageous to the transfer of photogenerated carriers to SnO_2. However, while $FAPbI_3$/NDI/SnO_2 yields an operational device, $FAPbI_3$/SnO_2 does not. This can be explained by the passivation and protection of the $FAPbI_3$ surface by NDI, despite the non-optimal coverage of the surface (Fig. S21). The first unoccupied levels of the NDI are located near the bottom of the conduction band of the perovskite, suggesting that the NDI layer can act as a surface passivator while favouring electron injection into SnO_2. Additionally, NDI creates a very thin layer between $FAPbI_3$ and SnO_2 with an optimal p_z molecular orbital orientation (Fig. S34b), which is expected to play a beneficial role for electron extraction. In contrast, the $FAPbI_3$/NI/SnO_2 interface shows a type-I energy level alignment, impeding electron injection into the SnO_2 layer and explaining the poor performance. In addition, the top of the valence band of SnO_2 is near the Fermi level, which may lead to a p-type SnO_2 surface, further hindering electron injection. Finally, the unoccupied levels of the NI are located above the perovskite conduction band, further impeding electron transport. As a result, a fullerene-free device is realised with NDI, with the main limiting factor being the low FF and series resistance, which can be optimised to achieve higher performances beyond this work. This highlights the potential of using electroactive molecular or LD perovskite materials for non-fullerene-based devices in photovoltaics in the future.

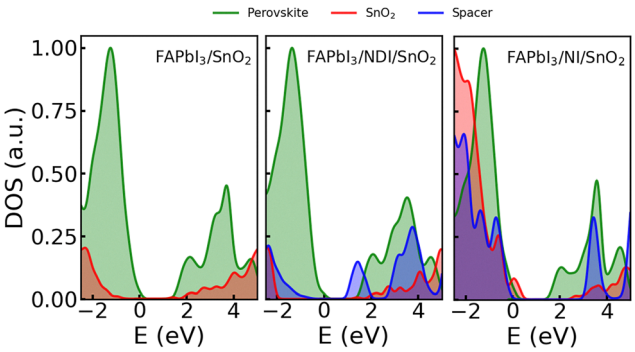

Fig. 5 Theoretical characteristics of fullerene-free perovskite interfaces. Projected density of states for $FAPbI_3$/SnO_2, $FAPbI_3$/NDI/SnO_2 and $FAPbI_3$/NI/SnO_2 with contributions from perovskite (green), NI/NDI spacers (blue) and SnO_2 (red). The energy is referenced to the calculated Fermi level (set to 0 eV), which corresponds to the calculated HOMO level. The projected density of states includes corrections to compensate for the absence of spin–orbit coupling and finite-size effects, as described in the SI.

The use of electroactive NDI/NI interlayers led to high performance over 20% of PCE, yet the champion performances were lower compared to small molecules with passivating effects, such as PDA,[8,49,56,57] which suggests the need for further optimisation. This was nonetheless expected to affect operational stability.[58] The evolution of the solar cell performance under continuous operating conditions showed that NI- and NDI-based devices maintained over 80% of their initial efficiency for more than 550 h, compared to both control and PDA-treated devices with T_{80} less than 500 h, showcasing enhanced stability and performance compared to the control (Fig. 6(a)). The increased operational stability can be partly associated with the increased hydrophobicity of the NI- or NDI-treated perovskite, confirmed by the static water contact angle measurement (Fig. 6(b)), improving the contacts with the charge-extraction layers and environmental stability, consistent with reports that enhanced hydrophobicity contributes to overall phase and operational stability beyond just moisture

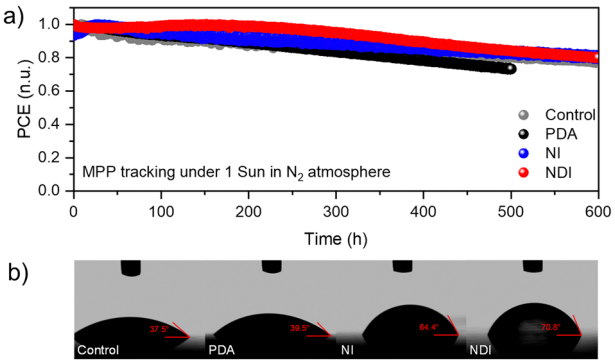

Fig. 6 Operational stability of inverted perovskite solar cell devices. (a) Maximum power point tracking evolution of the unencapsulated device under full solar illumination (AM 1.5 G, 100 mW cm^{-2} under nitrogen). (b) Contact angle measurements with a water droplet for the films.

protection.[59] This stimulates further investigation to optimise material design and device performance for inverted photovoltaics[60] in the future.

Conclusions

In summary, we demonstrated the formation of low-dimensional perovskite phases incorporating electroactive naphthalimide (NI) and naphthalenediimide (NDI) based moieties, through a combination of X-ray diffraction, GIWAXS, optoelectronic characteristics, and theoretical calculations. We applied the organic cations at the interface with 3D perovskites in inverted (p–i–n) perovskite solar cell devices to modify or replace fullerene-based ETLs. In the presence of fullerene-based ETL, both NI- and NDI-based systems showed higher PCE than the control, with NI having comparable efficiency to optimized non-electroactive PDA-based devices. The impact of the electroactive characteristics of NDI and the passivation effects of both NDI and NI were assessed by TRPL and PLQY measurements. Finally, fullerene-free devices based on NDI/ALD-SnO_2 layer were achieved, exhibiting a promising efficiency over 12%, showcasing NDI as an effective electron-extracting interlayer that can be further optimized. The resulting materials also improved operational stabilities, highlighting the potential of non-fullerene alternatives to advance perovskite solar cells.

Author contributions

The project was conceptualised by J. V. M., F. T. E., and M. G., who supervised the synthesis and characterisation of materials, conducted by M. N., P. N., T. A. C. and G. A., with support from L.P. The project was led by K. K. A. and G. A., who fabricated and characterised the materials under the supervision of S. M. Z., L. P., and F. E. T. Perovskite devices were fabricated by K. K. A., with support from L.Z. and J. K. Support on atomic layer deposition was provided by J. K. Additionally, P. Z. and G. A. carried out the GIWAXS measurements and analysis under the supervision of A. H. and F. S. The PL analysis of the films, fabricated and measured by K. K. A., was performed by F. T. E. DFT calculations and molecular dynamics simulations, along with their analysis and interpretation, were led by A. V., supported by N. L., V. S., V. C., and U. R., while F. T. E., J. V. M. and M. G. directed the study. All authors contributed to the manuscript and discussions.

Conflicts of interest

The authors declare no conflict of interest.

Data availability

Data can be accessed at DOI: **https://doi.org/10.5281/zenodo.14834415**, and it is available under the license CC-BY-4.0 (Creative Commons Attribution-ShareAlike 4.0 International). This involves structural and optoelectronic characterisation, as well as theoretical calculation datasets in the article and the SI. See DOI: **https://doi.org/10.1039/d5tc01418b**

Acknowledgements

This project is supported by the Swiss National Science Foundation (SNSF) PRIMA grant no. 193174. Parts of the research were performed at the ESRF (Grenoble, France) at ID10 and BM01 beamlines. We acknowledge the support of Dr Oleg Konovalov from the ID10 beamline (ESRF) and Dr Dmitry Chernyshov from the BM01 beamline (ESRF). We would also like to thank Dr Laura Piveteau (ISIC-NMRP, EPFL) for her support with solid-state NMR spectroscopy, Dr Mounir Driss Mensi for his support with XPS measurements, Dr Wenzhe Niu (ISIC-LPI, EPFL) for his support with compound characterisation, and Dr Mingyang Wei (ISIC-LPI, EPFL) for helpful discussions. We further acknowledge funding from the BMBF (ERUM-Pro) project 05K19VTA and thank Lena Merten and Leonard Simeonov for their experimental support. U.R. acknowledges the SNSF (grant no. 200020_219440). A. V., V. C. and U. R. acknowledge computational resources from the Swiss National Computing Centre CSCS.

References

1 A. K. Jena, A. Kulkarni and T. Miyasaka, *Chem. Rev.*, 2019, **119**, 3036–3103.
2 C. C. Stoumpos, C. D. Malliakas and M. G. Kanatzidis, *Inorg. Chem.*, 2013, **52**, 9019–9038.
3 A. Miyata, A. Mitioglu, P. Plochocka, O. Portugall, J. T.-W. Wang, S. D. Stranks, H. J. Snaith and R. J. Nicholas, *Nat. Phys.*, 2015, **11**, 582–587.
4 C. S. Ponseca, T. J. Savenije, M. Abdellah, K. Zheng, A. Yartsev, T. Pascher, T. Harlang, P. Chabera, T. Pullerits, A. Stepanov, J.-P. Wolf and V. Sundström, *J. Am. Chem. Soc.*, 2014, **136**, 5189–5192.

5 G. Xing, N. Mathews, S. Sun, S. S. Lim, Y. M. Lam, M. Grätzel, S. Mhaisalkar and T. C. Sum, *Science*, 2013, **342**, 344–347.
6 S. D. Stranks, G. E. Eperon, G. Grancini, C. Menelaou, M. J. P. Alcocer, T. Leijtens, L. M. Herz, A. Petrozza and H. J. Snaith, *Science*, 2013, **342**, 341–344.
7 A. Kojima, K. Teshima, Y. Shirai and T. Miyasaka, *J. Am. Chem. Soc.*, 2009, **131**, 6050–6051.
8 H. Chen, C. Liu, J. Xu, A. Maxwell, W. Zhou, Y. Yang, Q. Zhou, A. S. R. Bati, H. Wan, Z. Wang, L. Zeng, J. Wang, P. Serles, Y. Liu, S. Teale, Y. Liu, M. I. Saidaminov, M. Li, N. Rolston, S. Hoogland, T. Filleter, M. G. Kanatzidis, B. Chen, Z. Ning and E. H. Sargent, *Science*, 2024, **384**, 189–193.
9 K. Domanski, J.-P. Correa-Baena, N. Mine, M. K. Nazeeruddin, A. Abate, M. Saliba, W. Tress, A. Hagfeldt and M. Grätzel, *ACS Nano*, 2016, **10**, 6306–6314.
10 K. Domanski, B. Roose, T. Matsui, M. Saliba, S.-H. Turren-Cruz, J.-P. Correa-Baena, C. R. Carmona, G. Richardson, J. M. Foster, F. De Angelis, J. M. Ball, A. Petrozza, N. Mine, M. K. Nazeeruddin, W. Tress, M. Grätzel, U. Steiner, A. Hagfeldt and A. Abate, *Energy Environ. Sci.*, 2017, **10**, 604–613.
11 C. C. Boyd, R. Cheacharoen, T. Leijtens and M. D. McGehee, *Chem. Rev.*, 2019, **119**, 3418–3451.
12 B. T. Van Gorkom, T. P. A. Van Der Pol, K. Datta, M. M. Wienk and R. A. J. Janssen, *Nat. Commun.*, 2022, **13**, 349.
13 S. Teale, M. Degani, B. Chen, E. H. Sargent and G. Grancini, *Nat. Energy*, 2024, **9**, 779–792.
14 J. V. Milić, *J. Mater. Chem. C*, 2021, **9**, 11428–11443.
15 A. A. Sutanto, N. Drigo, V. I. E. Queloz, I. Garcia-Benito, A. R. Kirmani, L. J. Richter, P. A. Schouwink, K. T. Cho, S. Paek, M. K. Nazeeruddin and G. Grancini, *J. Mater. Chem. A*, 2020, **8**, 2343–2348.
16 Y. Bai, S. Xiao, C. Hu, T. Zhang, X. Meng, H. Lin, Y. Yang and S. Yang, *Adv. Energy Mater.*, 2017, **7**, 1701038.
17 J. Cho, J. T. DuBose, A. N. T. Le and P. V. Kamat, *ACS Mater. Lett.*, 2020, **2**, 565–570.
18 A. Thote, I. Jeon, J.-W. Lee, S. Seo, H.-S. Lin, Y. Yang, H. Daiguji, S. Maruyama and Y. Matsuo, *ACS Appl. Energy Mater.*, 2019, **2**, 2486–2493.
19 P. Gao, A. R. Bin Mohd Yusoff and M. K. Nazeeruddin, *Nat. Commun.*, 2018, **9**, 5028.
20 I. C. Smith, E. T. Hoke, D. Solis-Ibarra, M. D. McGehee and H. I. Karunadasa, *Angew. Chem., Int. Ed.*, 2014, **53**, 11232–11235.
21 J. Wei, Q. Wang, J. Huo, F. Gao, Z. Gan, Q. Zhao and H. Li, *Adv. Energy Mater.*, 2021, **11**, 2002326.
22 S. Foo, M. Thambidurai, P. Senthil Kumar, R. Yuvakkumar, Y. Huang and C. Dang, *Int. J. Energy Res.*, 2022, **46**, 21441–21451.
23 H. K. H. Lee, A. M. Telford, J. A. Röhr, M. F. Wyatt, B. Rice, J. Wu, A. De Castro Maciel, S. M. Tuladhar, E. Speller, J. McGettrick, J. R. Searle, S. Pont, T. Watson, T. Kirchartz, J. R. Durrant, W. C. Tsoi, J. Nelson and Z. Li, *Energy Environ. Sci.*, 2018, **11**, 417–428.
24 D. Yang, X. Zhang, K. Wang, C. Wu, R. Yang, Y. Hou, Y. Jiang, S. Liu and S. Priya, *Nano Lett.*, 2019, **19**, 3313–3320.
25 H. Yi, G. Zeng, C. Lai, D. Huang, L. Tang, J. Gong, M. Chen, P. Xu, H. Wang, M. Cheng, C. Zhang and W. Xiong, *Chem. Eng. J.*, 2017, **330**, 134–145.
26 D. Moia and J. Maier, *ACS Energy Lett.*, 2021, **6**, 1566–1576.
27 F. Jin, C. Liu, F. Hou, Q. Song, Z. Su, B. Chu, P. Cheng, H. Zhao and W. Li, *Sol. Energy Mater. Sol. Cells*, 2016, **157**, 510–516.
28 C. Xie, C. Zhou, B. Yang, L. Shen, L. Ke, L. Ding and Y. Yuan, *Appl. Phys. Express*, 2019, **12**, 064006.
29 G. Liu, X. Xie, X. Xu, Y. Wei, F. Zeng and Z. Liu, *Org. Electron.*, 2018, **62**, 189–194.
30 V. Sharma, J. D. B. Koenig and G. C. Welch, *J. Mater. Chem. A*, 2021, **9**, 6775–6789.
31 M. A. Jameel, T. C.-J. Yang, G. J. Wilson, R. A. Evans, A. Gupta and S. J. Langford, *J. Mater. Chem. A*, 2021, **9**, 27170–27192.
32 A. H. Proppe, M.-H. Tremblay, Y. Zhang, Z. Yang, R. Quintero-Bermudez, S. O. Kelley, S. Barlow, S. R. Marder and E. H. Sargent, *J. Phys. Chem. C*, 2020, **124**, 24379–24390.
33 A. Mishra, P. Ahlawat, G. C. Fish, F. Jahanbakhshi, M. Mladenović, M. Almalki, M. A. Ruiz-Preciado, M. C. Gelvéz-Rueda, D. J. Kubicki, P. A. Schouwink, V. Dufoulon, T. Schneeberger, A. Aslanzadeh, F. C. Grozema, S. M. Zakeeruddin, J.-E. Moser, U. Rothlisberger, L. Emsley, J. V. Milić and M. Grätzel, *Chem. Mater.*, 2021, **33**, 6412–6420.
34 S. Nussbaum, E. Socie, L. Yao, J.-H. Yum, J.-E. Moser and K. Sivula, *Chem. Mater.*, 2022, **34**, 3798–3805.
35 Z. Feng, X. Liu, K. Imaoka, T. Ishii, G. Tumen-Ulzii, X. Tang, G. F. Harrington, B. Heinrich, J.-C. Ribierre, L.-M. Chamoreau, L. Sosa Vargas, D. Kreher, K. Goushi, T. Matsushima, G. Zhou, F. Mathevet and C. Adachi, *Adv. Opt. Mater.*, 2023, **11**, 2202734.
36 S. Yang, D. Wu, W. Gong, Q. Huang, H. Zhen, Q. Ling and Z. Lin, *Chem. Sci.*, 2018, **9**, 8975–8981.
37 K. Ema, M. Inomata, Y. Kato, H. Kunugita and M. Era, *Phys. Rev. Lett.*, 2008, **100**, 257401.
38 S. Nussbaum, E. Socie, G. C. Fish, N. J. Diercks, H. Hempel, D. Friedrich, J.-E. Moser, J.-H. Yum and K. Sivula, *Chem. Sci.*, 2023, **14**, 6052–6058.
39 M.-H. Tremblay, A. M. Zeidell, S. Rigin, C. Tyznik, J. Bacsa, Y. Zhang, K. Al Kurdi, O. D. Jurchescu, T. V. Timofeeva, S. Barlow and S. R. Marder, *Inorg. Chem.*, 2020, **59**, 8070–8080.
40 Y. Li, J. V. Milić, A. Ummadisingu, J.-Y. Seo, J.-H. Im, H.-S. Kim, Y. Liu, M. I. Dar, S. M. Zakeeruddin, P. Wang, A. Hagfeldt and M. Grätzel, *Nano Lett.*, 2019, **19**, 150–157.
41 M. C. Gélvez-Rueda, P. Ahlawat, L. Merten, F. Jahanbakhshi, M. Mladenović, A. Hinderhofer, M. I. Dar, Y. Li, A. Dučinskas, B. Carlsen, W. Tress, A. Ummadisingu, S. M. Zakeeruddin, F. Schreiber, A. Hagfeldt, U. Rothlisberger, F. C. Grozema, J. V. Milić and M. Graetzel, *Adv. Funct. Mater.*, 2020, **30**, 2003428.
42 G. Grancini and M. K. Nazeeruddin, *Nat. Rev. Mater.*, 2019, **4**, 4–22.
43 L. Mao, C. C. Stoumpos and M. G. Kanatzidis, *J. Am. Chem. Soc.*, 2018, **141**, 1171–1190.

44 J. V. Milić, S. M. Zakeeruddin and M. Grätzel, *Acc. Chem. Res.*, 2021, **54**, 2729–2740.
45 M. Almalki, M. H. Alotaibi, A. Q. Alanazi, F. T. Eickemeyer, S. M. Alenzi, Y. A. Alzahrani, L. Piveteau, A. Y. Alymani, A. Albadri, H. Albrithen, J. V. Milić, S. M. Zakeeruddin, H. Zhang and M. Grätzel, *Adv. Funct. Mater.*, 2024, **34**, 2309789.
46 D. J. Kubicki, D. Prochowicz, A. Hofstetter, S. M. Zakeeruddin, M. Grätzel and L. Emsley, *J. Am. Chem. Soc.*, 2017, **139**, 14173–14180.
47 A. Q. Alanazi, M. H. Almalki, A. Mishra, D. J. Kubicki, Z. Wang, L. Merten, F. T. Eickemeyer, H. Zhang, D. Ren, A. Y. Alyamani, H. Albrithen, A. Albadri, M. H. Alotaibi, A. Hinderhofer, S. M. Zakeeruddin, F. Schreiber, A. Hagfeldt, L. Emsley, J. V. Milić and M. Graetzel, *Adv. Funct. Mater.*, 2021, **31**, 2101163.
48 T. Soto-Montero, S. Kralj, R. Azmi, M. A. Reus, J. S. Solomon, D. M. Cunha, W. Soltanpoor, D. S. Utomo, E. Ugur, B. Vishal, M. Ledinsky, P. Müller-Buschbaum, F. Babbe, D. K. Lee, C. M. Sutter-Fella, E. Aydin, S. De Wolf and M. Morales-Masis, *Joule*, 2024, **8**, 3412–3425.
49 H. Chen, A. Maxwell, C. Li, S. Teale, B. Chen, T. Zhu, E. Ugur, G. Harrison, L. Grater, J. Wang, Z. Wang, L. Zeng, S. M. Park, L. Chen, P. Serles, R. A. Awni, B. Subedi, X. Zheng, C. Xiao, N. J. Podraza, T. Filleter, C. Liu, Y. Yang, J. M. Luther, S. De Wolf, M. G. Kanatzidis, Y. Yan and E. H. Sargent, *Nature*, 2023, **613**, 676–681.
50 C. Liu, Y. Yang, H. Chen, J. Xu, A. Liu, A. S. R. Bati, H. Zhu, L. Grater, S. S. Hadke, C. Huang, V. K. Sangwan, T. Cai, D. Shin, L. X. Chen, M. C. Hersam, C. A. Mirkin, B. Chen, M. G. Kanatzidis and E. H. Sargent, *Science*, 2023, **382**, 810–815.
51 J. Wang, L. Zeng, D. Zhang, A. Maxwell, H. Chen, K. Datta, A. Caiazzo, W. H. M. Remmerswaal, N. R. M. Schipper, Z. Chen, K. Ho, A. Dasgupta, G. Kusch, R. Ollearo, L. Bellini, S. Hu, Z. Wang, C. Li, S. Teale, L. Grater, B. Chen, M. M. Wienk, R. A. Oliver, H. J. Snaith, R. A. J. Janssen and E. H. Sargent, *Nat. Energy*, 2024, **9**, 70–80.
52 T. Kirchartz, J. A. Márquez, M. Stolterfoht and T. Unold, *Adv. Energy Mater.*, 2020, **10**, 1904134.
53 S. You, F. T. Eickemeyer, J. Gao, J.-H. Yum, X. Zheng, D. Ren, M. Xia, R. Guo, Y. Rong, S. M. Zakeeruddin, K. Sivula, J. Tang, Z. Shen, X. Li and M. Grätzel, *Nat. Energy*, 2023, **8**, 515–525.
54 M. J. Trimpl, A. D. Wright, K. Schutt, L. R. V. Buizza, Z. Wang, M. B. Johnston, H. J. Snaith, P. Müller-Buschbaum and L. M. Herz, *Adv. Funct. Mater.*, 2020, **30**, 2004312.
55 Q. Han, Y. Bai, J. Liu, K. Du, T. Li, D. Ji, Y. Zhou, C. Cao, D. Shin, J. Ding, A. D. Franklin, J. T. Glass, J. Hu, M. J. Therien, J. Liu and D. B. Mitzi, *Energy Environ. Sci.*, 2017, **10**, 2365–2371.
56 S. M. Park, M. Wei, J. Xu, H. R. Atapattu, F. T. Eickemeyer, K. Darabi, L. Grater, Y. Yang, C. Liu, S. Teale, B. Chen, H. Chen, T. Wang, L. Zeng, A. Maxwell, Z. Wang, K. R. Rao, Z. Cai, S. M. Zakeeruddin, J. T. Pham, C. M. Risko, A. Amassian, M. G. Kanatzidis, K. R. Graham, M. Grätzel and E. H. Sargent, *Science*, 2023, **381**, 209–215.
57 R. Azmi, D. S. Utomo, B. Vishal, S. Zhumagali, P. Dally, A. M. Risqi, A. Prasetio, E. Ugur, F. Cao, I. F. Imran, A. A. Said, A. R. Pininti, A. S. Subbiah, E. Aydin, C. Xiao, S. I. Seok and S. De Wolf, *Nature*, 2024, **628**, 93–98.
58 C. Liu, Y. Yang, H. Chen, I. Spanopoulos, A. S. R. Bati, I. W. Gilley, J. Chen, A. Maxwell, B. Vishal, R. P. Reynolds, T. E. Wiggins, Z. Wang, C. Huang, J. Fletcher, Y. Liu, L. X. Chen, S. De Wolf, B. Chen, D. Zheng, T. J. Marks, A. Facchetti, E. H. Sargent and M. G. Kanatzidis, *Nature*, 2024, **633**, 359–364.
59 G. Wu, H. Li, S. Chen, S. Liu, Y. Zhang and D. Wang, *Nanomaterials*, 2022, **12**, 3881.
60 D. Gao, B. Li, Q. Liu, C. Zhang, Z. Yu, S. Li, J. Gong, L. Qian, F. Vanin, K. Schutt, M. A. Davis, A. F. Palmstrom, S. P. Harvey, N. J. Long, J. M. Luther, X. C. Zeng and Z. Zhu, *Science*, 2024, **386**, 187–192.